Applied Mathematical Modelling 36 (2012) 4728–4741

Contents lists available at SciVerse ScienceDirect

Applied Mathematical Modelling

journal homepage: www.elsevier.com/locate/apm

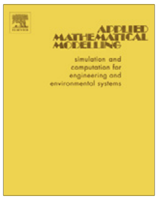

The modelling of an electromagnetic energy harvesting architecture

A.G. Avila Bernal *, L.E. Linares García

Centro de Microelectrónica (CMUA), Departamento de Ingeniería Eléctrica y Electrónica, Universidad de los Andes, Carrera 1E #19A-40, Bogotá D.C., Colombia

ARTICLE INFO

Article history:
Received 11 January 2011
Received in revised form 19 November 2011
Accepted 4 December 2011
Available online 24 December 2011

Keywords:
Energy harvesting
Electromagnetic generators
Magnetostatics
Finite Element Analysis

ABSTRACT

In this paper a detailed mathematical model for an electromagnetic energy harvesting architecture based on a semi-analytical approach is introduced. This model estimates the generated energy of the architecture by computing the static and dynamic magnetic and electric fields that describe its dynamics. A comparison of the static fields with the results of a Finite Element Analysis simulation in COMSOL Multiphysics shows good agreement. The model also features increased accuracy and numerical stability. In the model the semi-analytical solutions for the electromagnetic damping force exerted by the induced current coil and the induced electromotive force on the coil provide additional insight into the interactions of electromagnetic induction and damping. Additionally, the energy estimation could be used as a figure of merit in an maximization process to identify the optimal dimensions of the energy harvester.

1. Introduction

The field of energy harvesting has been actively researched for many decades [1], exploring the different physical phenomena that can be harnessed in order to generate useful electrical energy out of wasted ambient or residual energy sources, such as ambient or machine vibrations, dissipated heat, etc. Such physical phenomena include, for example, the photoelectric effect, piezoelectricity, magnetic induction and thermoelectricity [2]. The harvesting architectures found in the literature of the field are manifold, and strongly depend on the physical mechanism by which the harvested energy is transduced into electricity. The usual methods of analyzing such physical mechanisms are FEA simulations and linear parametric models, such as ANSYS simulations of an electromagnetic micro-power generator [3], COMSOL simulations of a self-powered thermal sensor [4], and linear models for several harvesting architectures [5–7]. In the case of electromagnetic architectures, even though Maxwell's equations are linear in the fields, the geometry of most of these architectures imposes boundary conditions that render the solutions nonlinear [8]. This has the following implications:

- Linear models of the architectures are only approximate.
- Accurate computation of the solutions by the FEA method requires significantly more computing power than linear models, and transient simulation is slow and unreliable, due to the changing mesh conditions generated by the moving parts of the architectures. Furthermore, static simulations can be hampered by artifacts that fail to disappear with increasingly fine meshes. An example of these artifacts is a verification of Newton's third law in a FEA simulation that is discussed within the text (see Section 4).

In this paper a different approach to model an electromagnetic harvesting architecture is discussed in detail. In Section 2 the underlying physical principles which the model is based on are decribed; Section 3 develops the mathematical model for

---

* Corresponding author. Tel.: +57 13394949; fax: +57 13324316.
E-mail addresses: a-avila@uniandes.edu.co (A.G. Avila Bernal), luis.linares@ieee.org (L.E. Linares García).

0307-904X/$ - see front matter © 2011 Elsevier Inc. All rights reserved.
doi:10.1016/j.apm.2011.12.007

Nomenclature

$\mathbf{x}$	observation or "test" coordinate for field observables
$\mathbf{x}'$	integration coordinate, used on every observable for adding the contribution from the infinitesimal elements involved in the calculation. In this paper, every primed object is to be referred to this integration coordinate
$\mathbf{B}$	magnetic field generated by some current distribution and/or a space region with remanent magnetization
$\mathbf{M}$	a space region with remanent magnetization
$\mathbf{H}$	magnetic field intensity
ρ, ϕ, z	the coordinates for the cylindrical coordinate system
$J_\nu(u)$	Bessel functions of the first kind and integer order ν
$sg(x)$	the sign-of-x function
$H(x)$	the Heaviside (or unit step) function
$\Pi(x;a)$	the boxcar function: $H(x) - H(x-a)$

the architecture's dynamics in a segregated fashion, one phenomenon at a time; the full model that includes all analyzed phenomena in Section 3.5 and finally some simulations are presented and discussed in Section 4. Some final comments are appended as well.

2. Geometry and dynamics of the harvesting architecture

In Fig. 1 the parameters that configure the geometry of an electromagnetic harvesting architecture are presented. Figure shows a rigid cylinder that contains three magnets, two of which are fixed and one of which is free to move. The motion of the free magnet is directed along the z axis, and is detected by a coil wound around the cylinder. The repulsive magnetic forces of the fixed magnets of the harvesting architecture maintain the free magnet in a position of equilibrium. This equilibrium position shifts in response to an external signal, which could be generated by routine human body movements (i.e. walking, jogging). The physical phenomena that play a relevant role in the dynamics of this harvesting architecture are shown in Fig. 2. Each of them relates to a section in this document, as follows:

- Dynamic magnetic field : the magnetic field emanated by a permanent cylindrical magnet is calculated in Section 3.1.
- Magnetic force of interaction: the repulsive force among any pair of the magnets in Fig. 1 is modelled in Section 3.2.
- Induced electromotive force: the magnetic induction on the coil due to the relative movement of the moving magnet is modelled in Section 3.3.

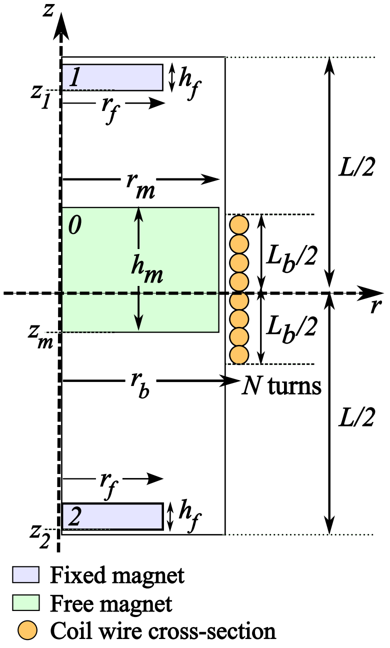

Fig. 1. Axi-symmetric cross section of the harvesting architecture, showing its geometrical parameters.

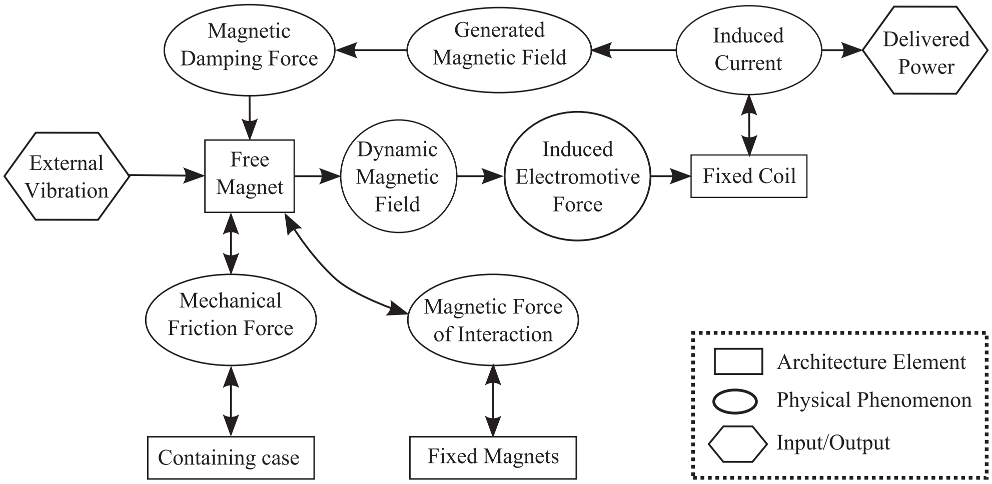

Fig. 2. Dynamics of the harvesting architecture as an interplay of physical phenomena. Arrow directions indicate causality relations.

- Coil's induced current : the electric current created by the induced electromotive force is discussed at the end of Section 3.3.
- Coil's generated magnetic field : the electric current mentioned before sets a magnetic field, which is calculated in Section 3.4.
- Magnetic damping force : the aforementioned magnetic field generated by the coil interacts with the moving magnet as described in Section 3.4.
- Mechanical damping force : the damping force due to friction between the moving magnet and the structure's cylinder is introduced in Section 3.5, which constructs the complete dynamical model of the harvester.

3. Modelling of the physical phenomena

3.1. The magnetic field of a cylindrical magnet

The harvesting architecture described in Section 2 exhibits cylindrical symmetry, hence its modelling is easiest done on the cylindrical coordinate system. For any of the magnets, the magnetostatic[1] scalar potential Φ_M ($\mathbf{x} = (\rho, \phi, z)$) associated to a permanent magnet (a space region with a remanent magnetization $\mathbf{M}$) is given by two terms: one volumetric and one surface [8]:

$$\Phi_M(\mathbf{x}) = -\frac{1}{4\pi}\int_V \frac{\nabla' \cdot \mathbf{M}(\mathbf{x}')}{|\mathbf{x}-\mathbf{x}'|} d^3x' + \frac{1}{4\pi}\oint_S \frac{\mathbf{M}(\mathbf{x}') \cdot \hat{n}'}{|\mathbf{x}-\mathbf{x}'|} d^2x'. \tag{3.1}$$

For the following, take the analyzed magnet to be magnet 0 in Fig. 1, fixed to the origin position ($z = 0$, that is, setting $z_m = 0$), with this magnet being homogeneously magnetized along the axial direction (so $\mathbf{M}(\mathbf{x}) = M_z(\mathbf{x})\hat{z} = M_0\Pi(\rho; r_m)\Pi(z; h_m)\hat{z}$). For the remaining surface term, the only surviving components of the integration are those located on the flat surfaces of the magnet ($z' = \{0, h_m\}$), where the surface normal vector $\hat{n}$ is equal to $\pm\hat{z}$, depending on the following cases:

$$\Phi_M(\mathbf{x}) = \frac{M_0}{4\pi}\left\{\int_{z'=h_m} - \int_{z'=0}\right\}\left(\frac{1}{|\mathbf{x}-\mathbf{x}'|}\rho' d\rho' d\phi'\right). \tag{3.2}$$

Notice the direct evaluation of $\Phi_M(\mathbf{x})$ as given in (3.2) for $\{\mathbf{x} \in \mathbb{R}^3 | \rho \neq 0\}$ gives rise to intricate and oscillatory expressions that demand numerical calculation, yielding long computation times. By exploiting the harvesting architecture's cylindrical axial symmetry, an exhaustive reduction in the number of these integrals is performed. Magnetostatic problems with cylindrical symmetry, such as the present one, admit an expression for the magnetic potential in terms of Bessel functions as given in (3.3) [8]. This $\Phi_M(\rho, z)$ has to be piecewise defined, so as to properly define the magnetic scalar potential for all ρ and z.

$$\Phi_M(\rho, z) = \begin{cases} \int_0^\infty F(k)e^{-kz}J_0(k\rho)dk, & z \geqslant h_m, \\ \int_0^\infty (G(k)e^{kz} + H(k)e^{-kz})J_0(k\rho)dk, & 0 < z < h_m, \\ \int_0^\infty I(k)e^{kz}J_0(k\rho)dk, & z \leqslant 0. \end{cases} \tag{3.3}$$

---

[1] The speed of any motion of this harvesting architecture is very small with respect to the speed of light, and so the quasistatic approximation of electromagnetism holds.

From the magnetic scalar potential $\Phi_M(\rho,z)$ the magnetic field **B** can be derived by means of relation (3.4).

$$\mathbf{B} = \mu(-\nabla\Phi_M + \mathbf{M}) \Rightarrow B_z = \mu\left(-\frac{\partial\Phi_M}{\partial z} + M_z\right). \tag{3.4}$$

For the continuity of the magnetic field the following boundary conditions are:

$$H_\rho(\rho, z = h^+) = H_\rho(\rho, z = h^-) \Rightarrow \left.\frac{\partial\Phi_M}{\partial\rho}\right|_{z=h^+} = \left.\frac{\partial\Phi_M}{\partial\rho}\right|_{z=h^-}, \tag{3.5a}$$

$$H_\rho(\rho, z = 0^+) = H_\rho(\rho, z = 0^-) \Rightarrow \left.\frac{\partial\Phi_M}{\partial\rho}\right|_{z=0^+} = \left.\frac{\partial\Phi_M}{\partial\rho}\right|_{z=0^-}. \tag{3.5b}$$

Applying (3.3)–(3.5) and solving for the unknown functions $F(k)$, $G(k)$, $H(k)$ and $I(k)$ (for details of this calculation, see Appendix A), the magnetic scalar potential for the magnet is obtained :

$$\Phi_M(\rho,z) = \frac{r_m M_0}{2}\int_0^\infty (e^{-k|z-h_m|} - e^{-k|z|})\frac{J_1(r_m k)J_0(k\rho)}{k}\, dk. \tag{3.6}$$

When the magnet is not located at the origin, and has been displaced a distance z_m (as shown in Fig. 1), the observation coordinate z needs to be transformed to the displaced coordinate system as $z \to z^* = z - z_m$. The magnetic field z-component $B_z(\rho,z)$, with this transformation applied, is obtained in (3.7).

$$B_z(\rho,z) = \mu M_z(\rho,z^*) + \frac{\mu M_0 r_m}{2}\int_0^\infty \left(e^{-k|z^*-h_m|} - sg(z^*)sg(z^*-h_m)e^{-k|z^*|}\right) \times J_1(kr_m)J_0(k\rho)\, dk. \tag{3.7}$$

For completeness, the ρ component of the magnetic field component $B_\rho(\rho,z)$ is also calculated by applying the rule $\mathbf{B} = \mu(-\nabla\Phi_M + \mathbf{M}) \Rightarrow B_\rho = -\mu\partial_\rho\,\Phi_M$ and proceeding as with (3.4). It is shown in (3.8).

$$B_\rho(\rho,z) = \frac{\mu M_0 r_m}{2}\int_0^\infty (e^{-k|z^*-h_m|} - e^{-k|z^*|})J_1(kr_m)J_1(k\rho)\, dk. \tag{3.8}$$

3.2. Magnetic force of interaction among two cylindrical magnets

The force exerted by an external magnetostatic field $\mathbf{B_e}$ on a magnet is given by the expression [8]:

$$\mathbf{F} = -\int_V (\nabla\cdot\mathbf{M})\mathbf{B_e}(\mathbf{x})d^3x + \oint_S (\mathbf{M}\cdot\hat{n})\mathbf{B_e}(\mathbf{x})d^2x.$$

In this case, the applied magnetic field is the one generated by a different magnet. For the calculation, consider magnets 0 and 1 in Fig. 1. Magnets 0 and 1 have axial magnetizations M_0 and M_1, respectively. Hence, the only remaining term is the surface integral:

$$\mathbf{F} = \oint_S (\mathbf{M}\cdot\hat{n}(\mathbf{x}))\mathbf{B_e}(\mathbf{x})d^2x. \tag{3.9}$$

Just like when calculating the magnetic field (see Section 3.1), the cylinder's upper and lower faces are the only ones contributing, as described in Section 3.1 above. Hence we obtain:

$$F_z = -M_0\left(\int_0^{r_f}\int_0^{2\pi}\mathbf{B_e}(\mathbf{x})d\theta\rho d\rho\bigg|_{z=z_1+h_f} - \int_0^{r_f}\int_0^{2\pi}\mathbf{B_e}(\mathbf{x})d\theta\rho d\rho\bigg|_{z=z_1}\right).$$

The field $\mathbf{B_e}$ in these integrals is the magnetic field produced by magnet 0, given in (3.7). Assuming the relative positions of these magnets are always as shown in figure, the field $\mathbf{B_e}$ is given by the expression valid for the upper region of magnet 0 (that is, the case $z_m + h_m < z_1$). Therefore the interaction force is calculated as follows:

$$\begin{aligned}
&\text{with } \gamma = \pi\mu_0 M_0 M_1 r_m :\\
&F_z(z_m,z_1) = \gamma\left(\int_0^{r_1}\int_0^\infty (e^{h_m k}-1)e^{k(z_m-z)}J_1(r_m k)J_0(k\rho)dk\bigg|_{z=z_1}\rho d\rho - \int_0^{r_1}\int_0^\infty (e^{h_m k}-1)e^{k(z_m-z)}J_1(r_m k)J_0(k\rho)dk\bigg|_{z=z_1+h_1}\rho d\rho\right)\\
&\qquad = \gamma r_1\left[\int_0^\infty (e^{h_m k}-1)e^{k(z_m-z_1)}\left(\frac{J_1(kr_m)J_1(kr_1)}{k}\right)dk - \int_0^\infty (e^{h_m k}-1)e^{k(z_m-z_1-h_1)}\left(\frac{J_1(kr_m)J_1(kr_1)}{k}\right)dk\right].
\end{aligned} \tag{3.10}$$

Conversely, if magnet 0 is placed over magnet 1 (that is, the case $z_m > z_1 + h_1$), the force can be calculated by exchanging $z_m \leftrightarrow z_1$ and $h_m \leftrightarrow h_1$ in (3.10). Such a situation applies for the interaction force among magnets 2 and 0.

3.3. Induced electromotive force on a cylindrical coil

As before, Fig. 1 depicts the geometry of the setup, where a coil with length L, density η of N turns per unit length and radius r_b surrounds a magnet with width h, radius r_m and axial, constant remanent magnetization M_0. For this setup, we fix the condition $r_b > r_m$. Starting from Faraday's law in integral form, for a fixed-shape circuit C whose normal vector $\mathbf{n}$ is oriented along the z axis ($\mathbf{n} = \hat{z}$), the induced electric field on the circuit is given by:

$$\oint_C \mathbf{E} \cdot d\mathbf{l} = -\int_S \frac{\partial \mathbf{B}}{\partial t} \cdot \mathbf{n}\, d^2x = -\int_S \frac{\partial B_z}{\partial t}\, d^2x,$$

where $\mathbf{B}$ is the magnet's generated magnetic field and C is a coil turn. For the magnet's equations of motion, note that the dynamic variable is z_m, and so the velocities relation is given by:

$$\dot{z} = -\dot{z_m}. \tag{3.11}$$

The change in the magnetic field is dictated by the magnet motion by means of relation (3.11):

$$\frac{\partial B_z}{\partial t} = \frac{\partial B_z}{\partial z}\frac{dz}{dt} = \frac{\partial B_z}{\partial z}\dot{z} = -\frac{\partial B_z}{\partial z}\dot{z}_m.$$

Replacing in the previous expression:

$$\oint_C \mathbf{E} \cdot d\mathbf{l} = \dot{z}_m \int_S \frac{\partial B_z}{\partial z}\, d^2x = \dot{z}_m \int_0^{r_B} \int_0^{2\pi} \frac{\partial B_z}{\partial z}\, d\theta \rho d\rho = 2\pi \dot{z}_m \int_0^{r_B} \frac{\partial B_z}{\partial z}\, \rho d\rho. \tag{3.12}$$

Applying (3.7), it becomes mandatory to treat separately the three exterior regions of the cylindrical magnet's generated magnetic field. Carrying out these calculations yields the result given in (3.13). For the details of the procedure, see Appendix B.

with $\alpha = \pi\mu_0\eta M_0 r_m r_b$ and $w(k, r_m, r_b) = \frac{J_1(r_m k) J_1(r_b k)}{k}$, for the cases of Table B.3 :

$$\mathcal{E}(z_m, \dot{z}_m) = \alpha \dot{z}_m \begin{cases} \vdots \\ \int_0^\infty f_i(k, z_m, h_m, L_b)\; w(k, r_m, r_b)\; dk \text{ case } i\,, \\ \vdots \end{cases} \tag{3.13}$$

with $i = \{1, \ldots, 5\}$:

$$f_1(k, z_m, h_m, L_b) = e^{-k(z_m + h_m + L_b/2)}(e^{h_m k} - 1)(e^{kL_b} - 1),$$
$$f_2(k, z_m, h_m, L_b) = [2 - e^{-k(z_m + h_m + L_b/2)}(-1 + e^{h_m k} + e^{kL_b} + e^{k(h_m + 2z_m)})],$$
$$f_3(k, z_m, h_m, L_b) = [e^{-k(z_m + h_m + L_b/2)}(1 + e^{2k(h_m + z_m)} - e^{k(h_m + 2z_m)} + e^{k(h_m + L_b + 2z_m)}) - 2],$$
$$f_4(k, z_m, h_m, L_b) = -e^{-k(L_b/2 - z_m)}(e^{h_m k} - 1)(e^{kL_b} - 1),$$
$$f_5(k, z_m, h_m, L_b) = e^{-k(z_m + h_m + L_b/2)}(e^{\min(h_m, L_b)k} - 1)(e^{k(h_m + 2z_m)} - 1).$$

This induced voltage $\mathcal{E}(z_m, \dot{z}_m)$ generates an induced current i_{ind} given by:

$$\mathcal{E}(z_m, \dot{z}_m) = (R_{\text{coil}} + R_{\text{load}})i_{\text{ind}} + L_{\text{coil}}\frac{di_{\text{ind}}}{dt}, \tag{3.14}$$

where R_{load} is the load resistance shunted to the coil, and R_{coil} and L_{coil} are the coil resistance and inductance, respectively. R_{load} models the device that is to be powered by this architecture. This induced current will establish a magnetic field on its own, concentrated mainly inside the coil, which will play the role of a damping mechanism that will decrease the magnet's speed as it moves through the coil. This mechanism is fundamentally a consequence of energy conservation, because had it not existed, an instantaneous excitation of the system would produce an infinite amount of energy over time. The next task is to calculate the generated magnetic field and the force it exerts on the magnet.

3.4. The magnetic field due to a current in a coil

The procedure shown in this section is done with respect to Fig. 1. In presence of applied (free) currents, the best way to proceed is by calculating the magnetic vector potential $\mathbf{A}$ and derive the observables through the relation $\mathbf{B} = \nabla \times \mathbf{A}$. Again, referring to [8] for setting our starting point, we begin with the following equation for the magnetic vector potential:

$$\mathbf{A}(\mathbf{x}) = \frac{\mu_0}{4\pi}\int \frac{\mathbf{J}(\mathbf{x}')}{|\mathbf{x} - \mathbf{x}'|}d^3x', \tag{3.22}$$

where the applied current density **J** must be cast in Cartesian coordinates in order to use this expression. For this geometry, there is only one free current, which flows in the angular (azimuthal) direction:

$$J_\phi(\mathbf{x}') = \eta I r_b \delta(\rho' - r_b)\Pi(z', -L_b/2, L_b/2),$$
$$\text{with } \Pi(z,a,b) = \begin{cases} 1 & a \leqslant z \leqslant b, \\ 0 & otherwise, \end{cases}$$

We express our total free current density as:

$$\mathbf{J}(\mathbf{x}') = -J_\phi \sin\phi' \hat{x} + J_\phi \cos\phi' \hat{y}.$$

Due to the axial symmetry, we can define the observation plane $\phi = 0$ for calculation purposes. Since integral (3.22) is symmetric about $\phi' = 0$, the x component will not contribute, and the only remaining component is y, which corresponds to the azimuthal component A_ϕ. That is, $\mathbf{A} = A_\phi \hat{\phi}$. The result, given in (3.23),

$$\begin{aligned} A_\phi(z,\rho) &= \frac{\mu_0}{4\pi}\int \frac{J_\phi(\mathbf{x}')\cos\phi'}{|\mathbf{x}-\mathbf{x}'|} d^3x' = \frac{\mu_0}{4\pi}\eta I r_b \int \frac{\delta(\rho' - r_b)\Pi(z', -L_b/2, L_b/2)\cos\phi'}{|\mathbf{x}-\mathbf{x}'|} d^3x' = \frac{\mu_0}{4\pi}\eta I r_b \int_0^{2\pi}\int_{-L_b/2}^{L_b/2} \frac{\cos\phi'}{|\mathbf{x}-\mathbf{x}'|} dz' d\phi', \\ A_\phi(z,\rho,L_b,r_b) &= \frac{\mu_0}{2\pi}\eta I r_b \int_0^{\pi} \log\left(\frac{f^+(\phi',\rho,z;r_b,L_b)}{f^-(\phi',\rho,z;r_b,L_b)}\right) d\phi', \\ &\text{with } f^\pm(\phi',\rho,z;r_b,L_b) = 2z \pm L_b + \sqrt{L_b^2 \pm 4L_b z + 4\left(r_b^2 + z^2 + \rho^2\right) - 8r_b\rho\cos\phi'} \end{aligned} \tag{3.23}$$

cannot be cast in closed form, requiring again to compute a 1D numerical integration for every point where it is required to find the value of the vector potential. The magnetic field components are derived through the fundamental relation, by means of the following expressions:

$$B_\rho = -\frac{\partial A_\phi}{\partial z} \qquad B_z = \frac{1}{\rho}\frac{\partial}{\partial \rho}(\rho A_\phi).$$

It is, however, not mandatory for our purposes to explicitly obtain these components, as we are only interested in computing the force exerted on the moving magnet, in the z direction. For this we use (3.9):

$$\begin{aligned} \mathbf{F} &= \oint_S (\mathbf{M}\cdot\hat{n}(\mathbf{x}))\mathbf{B_e}(\mathbf{x})\ d^2x = \int_{\text{Upper face}} (\mathbf{M}\cdot\hat{n}(\mathbf{x}))\mathbf{B_e}(\mathbf{x})\ d^2x - \int_{\text{Lower face}} (\mathbf{M}\cdot\hat{n}(\mathbf{x}))\mathbf{B_e}(\mathbf{x})\ d^2x, \\ F_z &= M_0\left(\int_0^{2\pi}\int_0^{r_m} \rho B_z(\mathbf{x})\Big|_{z=z_m+h_m} d\rho d\phi - \int_0^{2\pi}\int_0^{r_m} \rho B_z(\mathbf{x})\Big|_{z=z_m} d\rho d\phi\right) \\ &= 2\pi M_0\left(\int_0^{r_m} \frac{\partial}{\partial\rho}(\rho A_\phi)\Big|_{z=z_m+h_m} d\rho - \int_0^{r_m} \frac{\partial}{\partial\rho}(\rho A_\phi)\Big|_{z=z_m} d\rho\right) \\ &= 2\pi M_0[(\rho A_\phi)(z_m+h_m,r_m,L_b,r_b) - (\rho A_\phi)(z_m+h_m,0,L_b,r_b) - (\rho A_\phi)(z_m,r_m,L_b,r_b) + (\rho A_\phi)(z_m,0,L_b,r_b)], \\ F_z &= 2\pi M_0\ r_m[A_\phi(z_m+h_m,r_m,L_b,r_b) - A_\phi(z_m,r_m,L_b,r_b)] \end{aligned} \tag{3.24}$$

and $A_\phi(z,\rho)$ is given by (3.23).

3.5. Dynamical equations of the harvester

The interplay of all physical interactions described in this paper is depicted in Fig. 2. Now an explicit representation of this interplay is required in order to simulate and analyze the harvesting device for a given set of its parameters. If the device is subject to an externally applied driving acceleration $A_d(t)$, the moving magnet's dynamics are given by (3.25):

$$\dot{z}_m = v_m, \tag{3.25a}$$

$$\dot{v}_m = \frac{F_{If1}(z_m) + F_{If2}(z_m) + F_{Ib}(z_m, i_{\text{ind}}) - f_r(v_m)}{m_m} - A_d(t), \tag{3.25b}$$

$$\dot{i}_{\text{ind}} = \frac{\mathcal{E}(z_m, v_m) - (R_{\text{coil}} + R_{\text{load}})i_{\text{ind}}}{L_{\text{coil}}}, \tag{3.25c}$$

where m_m is the moving magnet's mass, F_{If1} and F_{If2} are given by (3.10) for the moving magnet interacting with each of the fixed magnets, F_{Ib} is given by (3.24), $\mathcal{E}(z_m, v_m)$ is as shown in (3.13) and $f_r(v_m)$ is the friction force due to the sliding of the moving magnet against its container wall. Note from (3.24) and (3.23) that $F_{Ib}(z_m, i_{\text{ind}}) \equiv F_{Ib}(z_m) \cdot i_{\text{ind}}$, and also from (3.13) it can be checked that $\mathcal{E}(z_m, v_m) \equiv \mathcal{E}(z_m) \cdot v_m$. Therefore (3.25) is transformed into:

$$\dot{z}_m = v_m, \tag{3.26a}$$

$$\dot{v}_m = \frac{F_{If1}(z_m) + F_{If2}(z_m) + i_{\text{ind}} F_{Ib}(z_m) - f_r(v_m)}{m_m} - A_d(t), \tag{3.26b}$$

$$\dot{i}_{\text{ind}} = \frac{v_m \mathcal{E}(z_m) - (R_{\text{coil}} + R_{\text{load}}) i_{\text{ind}}}{L_{\text{coil}}}. \tag{3.26c}$$

A further effort can be undertaken by studying the scaling properties of the $F_I(z), \mathcal{E}(z)$ and $F_{Ib}(z)$ functions, which besides revealing some of their relevant theoretical characteristics, allows for improved numerical conditioning of their calculation as well as of the integration of the ODE system (3.26) through time, by scaling its equations. From (3.10) and (3.13) it can be seen that $F_I(z)$ and $\mathcal{E}(z)$ can be written as specific cases of a function $g(z)$ given by:

$$g(a, b, c) = \sum_{i=1}^{N} \beta_i T_{v_i}^{(\mu_i)}(a_i, b_i, c_i), \tag{3.27}$$

$$T_v^{(\mu)}(a, b, c) = \int_0^\infty e^{-ak} J_1(bk) J_v(ck) k^\mu \, dk, \tag{3.28}$$

with N a positive integer, β_i a real constant, a_i, b_i and c_i real positive constants and $v_i \in \{0,1\}$, $\mu_i \in \{0, -1\}$. By performing the change of variable $k = \lambda k'$ for some positive real constant λ, it can be shown that:

$$T_v^{(\mu)}(a, b, c) = \lambda^{\mu+1} T_v^{(\mu)}(\lambda a, \lambda b, \lambda c). \tag{3.29}$$

Matching the expressions (3.10) and (3.13) with the form in (3.27) reveals that for both $F_I(z)$ and $\mathcal{E}(z)$, their associated g_{F_I} and $g_{\mathcal{E}}$ have all of their $v_i = 1$ and $\mu_i = -1$, which in view of (3.29) indicates that:

$$\mathcal{E}(\lambda z_m, \lambda r_m, \lambda h_m, \lambda r_b, \lambda L_b) = \mathcal{E}(z_m, r_m, h_m, r_b, L_b), \tag{3.30}$$

$$F_I(\lambda z_m, \lambda r_m, \lambda h_m, \lambda z_1, \lambda r_1, \lambda h_1) = F_I(z_m, r_m, h_m, z_1, r_1, h_1). \tag{3.31}$$

From (3.24) and (3.23) it is evident that:

$$\lambda^2 F_{Ib}(\lambda z_m, \lambda r_m, \lambda h_m, \lambda L_b, \lambda r_b) = F_{Ib}(z_m, r_m, h_m, L_b, r_b) \tag{3.32}$$

because the integrand in (3.23) is invariant with respect to the λ-scaling and there are two scaled variables (r_m and r_b) as global factors of F_{Ib}.

The introduction of the g(z) functions in (3.27) (which will be called from now on *geometric functions*) and their associated *geometric factor* $T_v^{(\mu)}(a, b, c)$ as descriptors of the physical fields of this harvesting architecture raises a practical issue in the numerical calculations for these fields: The computation of $T_v^{(\mu)}(a, b, c)$ comprises a semi-infinite integral with a highly oscillatory integrand. There are widely known techniques (i.e. Gauss-Kronrod quadrature [9]) that can handle these kinds of integrals, but the computation is not unconditionally stable, as was evidenced in experiments with the `quadgk` function in MATLAB. This geometric factor $T_v^{(\mu)}(a, b, c)$ must exist for every value in its parameter ranges as set previously, but that did not always hold when experimenting with the aforementioned integration routine. Hence, an analytical transformation of $T_v^{(\mu)}(a, b, c)$ is required such that the existence for all values in the specified parameter ranges is assured. This transformation begins by employing one of the many representations for integer order Bessel functions[10]:

$$\begin{aligned} T_v^{(\mu)}(a, b, c) &= \int_0^\infty e^{-ak} J_1(bk) \left(\frac{1}{2\pi} \int_0^{2\pi} e^{ick\sin\theta - iv\theta} d\theta \right) k^\mu dk = \frac{1}{2\pi} \int_0^{2\pi} d\theta e^{-iv\theta} \int_0^\infty e^{-(a - ic\sin\theta)k} J_1(bk) k^\mu dk \\ &= \frac{1}{2\pi} \int_0^{2\pi} d\theta e^{-iv\theta} \mathcal{H}_1 \{ e^{-(a - ic\sin\theta)k} k^{\mu-1} \}, \end{aligned} \tag{3.33}$$

where $\mathcal{H}_1$ is the Hankel transform of order 1 from k into b. This particular transform is an elementary function for the cases $\mu \in \{0, -1\}$:

$$T_v^{(\mu)}(a, b, c) = \begin{cases} \frac{1}{2\pi b} \int_0^{2\pi} d\theta e^{-iv\theta} \left[1 - \left(1 + \frac{b^2}{(a - ic\sin\theta)^2} \right)^{-1/2} \right] & \mu = 0, \\ \frac{1}{2\pi b} \int_0^{2\pi} d\theta e^{-iv\theta} (a - ic\sin\theta) \left[1 - \sqrt{1 + \frac{b^2}{(a - ic\sin\theta)^2}} \right] & \mu = -1. \end{cases}$$

Testing the parity and periodicity of the integrand in (3.33) with respect to θ reveals a periodicity of 2π, which is even in its real part and odd in its imaginary part. Hence the imaginary part vanishes, and the full integral is always real as expected from the start of the transformation procedure. Therefore:

$$T_{\nu}^{(\mu)}(a,b,c)=\begin{cases}\frac{1}{\pi b}\int_0^{\pi}d\theta e^{-i\nu\theta}\left[1-\left(1+\frac{b^2}{(a-ic\sin\theta)^2}\right)^{-1/2}\right] & \mu=0,\\ \frac{1}{\pi b}\int_0^{\pi}d\theta e^{-i\nu\theta}(a-ic\sin\theta)\left[1-\sqrt{1+\frac{b^2}{(a-ic\sin\theta)^2}}\right] & \mu=-1.\end{cases}\tag{3.34}$$

A special simple case is [10]:

$$T_1^{(-1)}(0,b,c)=\frac{\min(b,c)}{2\max(b,c)}.\tag{3.35}$$

The accuracy and numerical stability of these integrals can be improved as follows. Define $\hat{c}=c/a,\ \hat{b}=b/a$, then:

$$T_{\nu}^{(\mu)}(a,b,c)=\begin{cases}\frac{1}{\pi b}\int_0^{\pi}d\theta e^{-i\nu\theta}\left[1-\left(1+\frac{\hat{b}^2}{(1-i\hat{c}\sin\theta)^2}\right)^{-1/2}\right] & \mu=0,\\ \frac{1}{\pi b}\int_0^{\pi}d\theta e^{-i\nu\theta}(1-i\hat{c}\sin\theta)\left[1-\sqrt{1+\frac{\hat{b}^2}{(1-i\hat{c}\sin\theta)^2}}\right] & \mu=-1.\end{cases}\tag{3.36}$$

These are finite integrals with a smooth non-oscillatory integrand, amenable to computation using almost any kind of numerical integration technique. Armed with these transformations and the scaling relations (3.31), (3.30) and (3.32), the ODE system (3.26) can be numerically integrated efficiently and reliably for any physically feasible set of geometrical parameters of the architecture.

4. Simulations of the harvester

4.1. Comparison of static fields calculations with simulations in COMSOL Multiphysics

Even though COMSOL Multiphysics v3.5a supports simulations with a moving mesh (as would be needed for a complete transient simulation of the harvesting architecture), every simulation attempted that included dynamics on a moving mesh failed. The cause for this failure is still an open question, pending feedback from COMSOL. Therefore, the static fields derived in this work have been simulated in the program, and a comparison is made between the results generated by COMSOL Multiphysics and those from the model so far developed. The simulations are executed in MATLAB.

4.1.1. Static fields comparisons

The static fields computed for comparison are the magnetic field generated by a cylindrical permanent magnet (see Section 3.1) and by a coil with a given applied current (see Section 3.4). The geometry and other physical parameters for each simulation are as follows:

- For the cylindrical magnet:
  - Radius r_m = 6.5 mm
  - Height h_m = 5 mm
  - Magnetization M_0 = 1.15 MA/m
- For the coil:
  - Radius r_b = 0.4 m
  - Height L_b = 1 m
  - Applied current density ηI = 1 A/m (Note this does not represent a setting where η = 1 turn/m and I = 1 A, as it is not consistent with the approximation of a densely wound coil. It rather represents a setting where, for example, η = 1000 turns/m and I = 1 mA)

In Fig. 3 some surface plots of the magnetic fields generated by the magnet and the coil are presented. The space grid points evaluated for the construction of these plots are the same for the COMSOL simulations and the model's computations. Hence, several quantitative comparisons can easily be undertaken. In Table 1 two sample comparison indices are computed: the absolute value of the maximum of the raw difference of both calculations (with this work's model and COMSOL Multiphysics) and the root of the mean squared error, integrated over the entire space grid. It can be observed that the agreement among the two calculations is very close, with the tightest one being the magnetic field generated by a coil. Overall, the static fields of the model are in good agreement the results of COMSOL Multiphysics, but the model provides more efficient means for the calculation, as it does not need meshing of the entire simulation space domain.

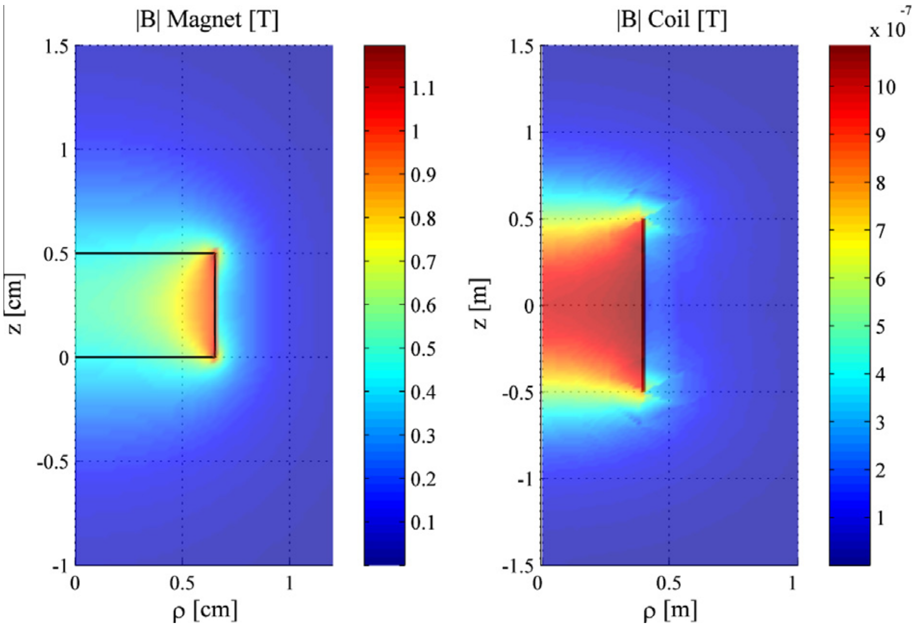

Fig. 3. Magnetic field magnitude for the static fields generated by a cylindrical magnet (left) and an applied current in a cylindrical coil (right). The black lines indicate the element's (magnet or coil) cross section boundary.

Table 1
Evaluation of two comparison indices for the COMSOL and model static field simulations.

Index	Permanent magnet			Coil with applied current		
	$\|\mathbf{B}\|$	B_ρ	B_z	$\|\mathbf{B}\|$	B_ρ	B_z
$\|\Delta\|$	0.0774	0.0773	0.0949	2.97e−7	3.25e−7	1.88e−7
RMSE	1.322e−9	1.914e−9	1.052e−9	4.92e−16	4.60e−16	3.60e−16

4.1.2. Physics verification

In verifying the results from the FEA simulations in COMSOL, an issue of physical accuracy and correspondence arose, when calculating the magnetic force of interaction (attraction or repulsion) among two magnets. For a sample setup, two magnets identical to the simulated in Fig. 3 are placed one above the other, with their axial axes aligned and separated by a distance of 1 cm, and with opposite magnetizations so as to repeal each other. A calculation of their mutual repulsion forces is generated by COMSOL, evaluated in both magnets. Newton's third law of motion requires these repulsion forces to be equal in magnitude and opposite in direction. Equivalently, their sum must be identically zero. The COMSOL results however yield a non-zero sum or mismatch with respect to the law, as detailed in Table 2. The magnitude of the sum seems to decrease, as well as the values of the forces themselves converge to the model's result, with increasing mesh detail, but due to the large computing resources demand of simulation with finer meshes, no further solutions have been calculated. This behaviour of the COMSOL simulation is consistent with previous results on FEA computation of electromagnetic forces and torques, since the various methods available in FEA converge only asymptotically to the physical value. These methods yield result mismatches among the methods of approximately 50% for low-density meshes [11]. Therefore, the presented analytical model, makes gains in accuracy and performance, through a loss in modelling generality and flexibility.

4.2. An efficient method for the integration of the model's dynamics

Recall from (3.26) how the fields F_{Ib} and $\mathcal{E}$, which are dependent on dynamic variables of the model besides the moving magnet's position, can be cast into product forms such that they can be precalculated independently of these dynamic variables, and then multiplied by the value of such dynamic variables at each particular time. That is, $F_I(z_m)$, $F_{Ib}(z_m)$ and $\mathcal{E}(z_m)$, through their geometric functions g_I, g_{Ib} and $g_{\mathcal{E}}$, can be put as high-resolution one-dimensional look-up tables for interpolation at simulation time, factorizing a set of complex calculations into a one-time procedure, and replacing it at simulation time with a highly optimized one, as is an 1D table look-up with linear interpolation. Performing a non-dimensionalizing scaling of the variables by means of (3.31), (3.30) and (3.32) (i.e. choosing $\lambda = l_c^{-1}$ with l_c a characteristic length scale like $L/2$ in Fig. 1), detailed parametric sensitivity analyses can be done independently of physical units, which optimizes the

Table 2
Verification of Newton's 3rd. Law compliance of COMSOL static simulation of two identical magnets placed one above the other. The last row shows the model result.

# Mesh elements	Forces [N]	N3L Mismatch [mN]
13513	1 → 2: 3.4560 2 → 1: −3.4663	−10.3
53748	1 → 2: 3.4473 2 → 1: −3.4603	−12.9
214992	1 → 2: 3.4669 2 → 1: −3.4731	−6.2
Model's result		
N/A	1 → 2: 3.4890 2 → 1: −3.4890	0

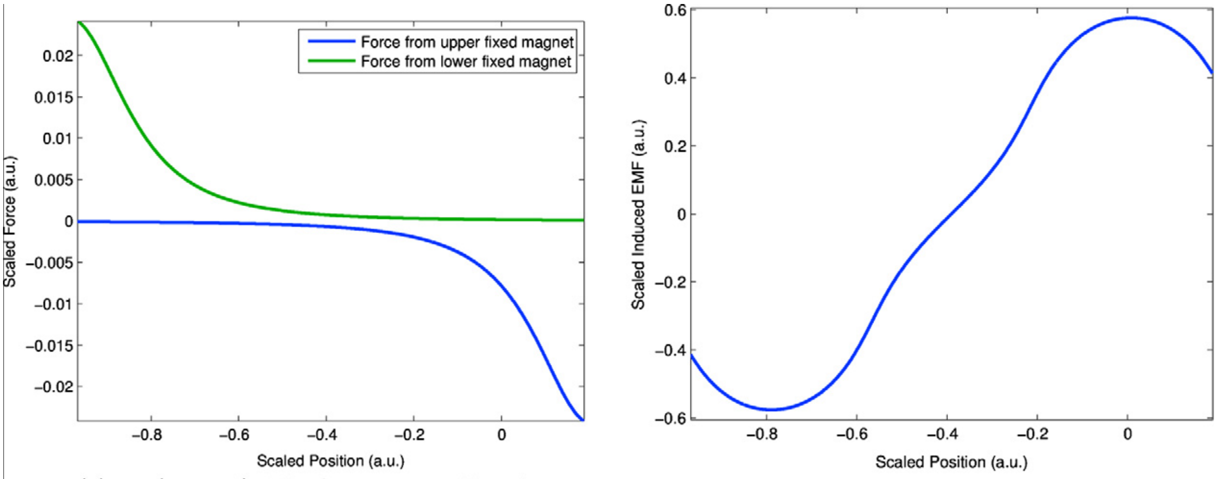

(a) g_{I_i} $(i = 1, 2)$, The forces exerted by the two non-identical fixed magnets

(b) $g_{\mathcal{E}}$, The induced EMF on the Coil

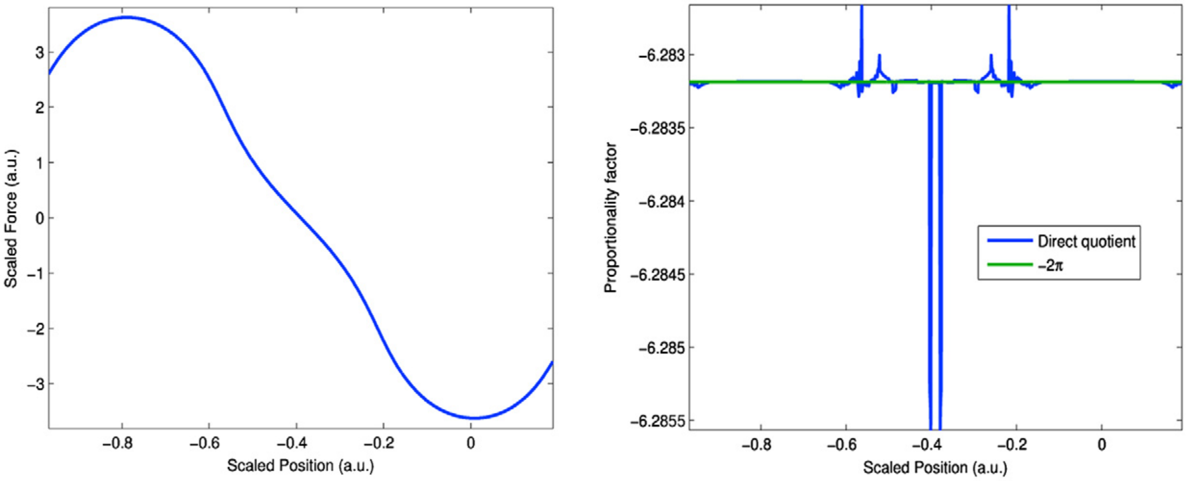

(c) g_{Ib}, The force exerted by the Coil

(d) $g_{Ib}/g_{\mathcal{E}}$, Electromagnetic ratio

Fig. 4. Look-up tables for the geometric functions g_I, g_{Ib} and $g_{\mathcal{E}}$ for a sample configuration, non-dimensionalized by the scaling $\lambda^{-1} = L/2$. The horizontal axes is λz_m, with z_m as in Fig. 1.

design flow for this harvesting architecture. Hence, for a sample set of physical parameters for the harvester, a plot of these look-up tables is given in Fig. 4, with 1000 points each. As it can be appreciated, the shapes depicted for these fields make the system nonlinear in nature, with several linearization points required if a piecewise-linear approximation is desired. In comparing the shapes of g_{Ib} and $g_{\mathcal{E}}$ it might come as a surprise their strong resemblance, and so their ratio, denominated the *electromagnetic induction ratio*, has been calculated for each corresponding entry of their look-up tables. The mean of this ratio is very close to -2π (with an absolute error of 10^{-5}), as shown in Fig. 4(d), and most importantly, it has been observed to be independent of the values of the geometrical parameters (by testing several different value sets of such parameters). Hence, this resemblance has a fundamental origin, very likely arising from the complementary role of the magnetic and electric fields in the phenomenon of electromagnetic induction.

4.3. Computing power considerations for the model and the FEA method

In view of the presented results, and particularly Section 4.1.2, it can be seen that the FEA method might require a fine mesh for accurate computation of all physical quantities of interest, such as potentials and forces. This in turn involves the solution of a linear system with a large number N of degrees of freedom, which is usually sparse [12], so the number of floating-point operations (FLOPs) it takes to solve it is of order N or N^2 worst-case [9]. This solution has to be computed for every position of the moving magnet, for a single set of parameters (i.e. dimensions and magnetization of the magnets, coil configuration and container size). Then, in order to generate the look-up tables (of size P), the number of FLOPs in the FEA method is of order NP. In contrast, the introduced model evaluates each of its geometric functions $g(a,b,c)$ (see Eq. (3.27)) with finite integrals, which are of order M in the number of FLOPs, with M the number of points where the integrands are evaluated. Hence, the computation of the look-up tables takes a number of FLOPs of order MP. The fundamental difference among the two methods is that virtually always $M \ll N$ (by at least an order of magnitude), for the same target accuracy. Therefore this model demands less computational power than the FEA method (in view of Section 4.1.2), at the loss of modelling generality and flexibility.

5. Conclusion

In this paper a mathematical model of an electromagnetic energy harvesting architecture has been discussed in detail. By specializing the geometry of the architecture (hence giving up modelling flexibility) this model allows calculation to arbitrary precision of the physical fields that govern the dynamics of the architecture with less computational power. By avoiding the discretization of the simulation domain, the accuracy of the described model is bounded only by the experimental uncertainties in the physical parameters of the architecture and the finite arithmetic precision of the computing platform. These features benefit the accuracy of the generated energy estimation that can be used as an optimization target to set the optimal dimensions of the presented energy harvesting architecture.

Appendix A. Calculation of the magnetic field produced by a cylindrical cylinder

Using (3.3) in (3.5) generates the following system of equations:

$$H(k) + G(k)e^{2kh} = F(k),$$
$$H(k) + G(k) = I(k).$$

Inverting the preceding system of equations:

$$H(k) = \frac{e^{2hk}I(k) - F(k)}{e^{2hk} - 1}, \tag{A.1}$$

$$G(k) = \frac{F(k) - I(k)}{e^{2hk} - 1}. \tag{A.2}$$

Now $F(k)$ and $I(k)$ must be calculated.

A.1. The magnetic field on the line r = 0

On this line the integral in (3.2) can be analytically calculated, with the result given in (A.3).

$$\begin{aligned}\Phi_M(0,z) &= \frac{M_0}{4\pi}\left(\int_0^{2\pi}\int_0^{r_m}\frac{\rho'}{\sqrt{(z-z')^2+\rho'^2}}d\rho' d\phi'\bigg|_{z'=h_m} - \int_0^{2\pi}\int_0^{r_m}((z-z')^2+\rho'^2)^{-1/2}\rho' d\rho' d\phi'\bigg|_{z'=0}\right)\\ &= \frac{1}{2}M_0\left(\sqrt{(h_m-z)^2+r_m^2} - \sqrt{r_m^2+z^2} - |h_m - z| + |z|\right)\end{aligned} \tag{A.3}$$

Then $\mathbf{B} = \mu_0(-\nabla\Phi_M + \mathbf{M})$ is derived. On the line $\rho = 0$ only the z component of the field survives, yielding the field on the entire axis $\rho = 0,\ \forall z \in \mathbb{R}$, as expressed in (A.4).

$$B_z(0,z) = -\mu_0\partial_z\Phi_M(0,z) = -\frac{1}{2}M_0\mu_0\left(\frac{z-h_m}{\sqrt{(h_m-z)^2+r_m^2}} - \frac{z}{\sqrt{r_m^2+z^2}}\right). \tag{A.4}$$

Employing relation (3.4) and evaluating on the line $\rho = 0$ we get:

$$B_z(0,z) = \begin{cases} \int_0^\infty [\mu_0 kF(k)]e^{-kz}dk & z \geqslant h_m, \\ \int_0^\infty [-\mu_0 kI(k)]e^{kz}dk & z \leqslant 0. \end{cases} \tag{A.5}$$

It can be noted from this result that $B_z(0,z)$ is the Laplace transform of the function $\mu_0 kF(k)$ for $z \geqslant h_m$ and likewise $B_z(0,-z)$ is about $-\mu_0 kI(k)$ for $z \leqslant 0$.

A.2. The inverse Laplace transforms

Using (A.4) and (A.5) the functions $F(k)$ and $I(k)$ can be calculated by using the inverse Laplace transform:

$$F(k) = -\frac{1}{2k}M_0(e^{h_m k} - 1)(\delta(k) - r_m J_1(r_m k)),$$
$$I(k) = -\frac{1}{2k}M_0(e^{-h_m k} - 1)(\delta(k) - r_m J_1(r_m k)).$$

These functions always appear as factors in integrands containing Bessel functions of the first kind, which vanish at the origin. Hence, the Dirac Delta term present in them unconditionally vanishes. Therefore, they do not contribute and can be taken out of these expressions:

$$F(k) = \frac{1}{2k}r_m M_0(e^{h_m k} - 1)J_1(r_m k), \tag{A.10}$$
$$I(k) = \frac{1}{2k}r_m M_0(e^{-h_m k} - 1)J_1(r_m k). \tag{A.11}$$

Using these results in (A.1) and (A.2):

$$H(k) = -\frac{1}{2k}r_m M_0 J_1(r_m k), \tag{A.12}$$
$$G(k) = \frac{1}{2k}r_m M_0 e^{-h_m k}J_1(r_m k). \tag{A.13}$$

A.3. The magnetic field at an arbitrary coordinate (r,z)

Invoking results (A.10), (A.11), (A.12) and (A.13) in (3.3), the expression for the magnetic scalar potential $\Phi(\rho,z)$ is obtained, as shown in (3.6).

Appendix B. Calculation of the induced electromotive force on the coil

In treating (3.12) for the space regions of (3.7), several cases for the induced electromotive force $\mathcal{E}$ arise, as given by (B.1). Their derivation is as follows:

- For $z \geqslant z_m + h_m$:

$$\oint_C \mathbf{E}\cdot d\mathbf{l} = 2\pi\dot{z}_m \int_0^{r_b} \frac{\partial}{\partial z}\left[\frac{1}{2}\mu_0 M_0 r_m \int_0^\infty (e^{h_m k} - 1)e^{k(z_m - z)}J_1(r_m k)J_0(k\rho)dk\right]\rho\, d\rho$$
$$= -\pi\mu_0 M_0 r_m r_b \dot{z}_m \int_0^\infty (e^{h_m k} - 1)e^{k(z_m - z)}J_1(r_m k)J_1(r_b k)\, dk.$$

- For $z_m < z < z_m + h_m$ (with $\rho > r_m$):

$$\oint_C \mathbf{E}\cdot d\mathbf{l} = 2\pi\dot{z}_m \int_0^{r_b} \frac{\partial}{\partial z}\left[-\frac{1}{2}\mu_0 M_0 r_m \int_0^\infty (e^{k(z_m - z)} + e^{k(z - h_m - z_m)})J_1(r_m k)J_0(k\rho)dk\right]\rho\, d\rho$$
$$= -\pi\mu_0 M_0 r_m r_b \dot{z}_m \times \int_0^\infty (e^{k(z - h_m - z_m)} - e^{k(z_m - z)})J_1(r_m k)J_1(r_b k)\, dk.$$

- For $z \leqslant z_m$:

$$\oint_C \mathbf{E}\cdot d\mathbf{l} = 2\pi\dot{z}_m \int_0^{r_b} \frac{\partial}{\partial z}\left[-\frac{1}{2}\mu_0 M_0 r_m \int_0^\infty (e^{-h_m k} - 1)e^{k(z - z_m)}J_1(r_m k)J_0(k\rho)dk\right]\rho d\rho$$
$$= -\pi\mu_0 M_0 r_m r_b \dot{z}_m \int_0^\infty (e^{-h_m k} - 1)e^{k(z - z_m)}J_1(r_m k)J_1(r_b k)dk.$$

These cases can be compactly expressed as follows:

$$\oint_C \mathbf{E}\cdot d\mathbf{l} = -\pi\mu_0 M_0 r_m r_b \dot{z}_m \int_0^\infty \left(e^{-k|z-h_m-z_m|} - e^{-k|z_m-z|}\right) J_1(r_m k) J_1(r_b k)\ dk. \tag{B.1}$$

This electromotive force induced by the moving magnet is for a single turn of the coil. Hence, the total electromotive force will be given by the equation:

$$\mathcal{E} = \eta\int_{-L_b/2}^{L_b/2} \frac{\partial\mathcal{E}}{\partial z}dz = \eta\int_{-L_b/2}^{L_b/2}\left(\oint_C \mathbf{E}\cdot d\mathbf{l}\right)dz = \eta\sum_i \int_{a_i}^{b_i}\left(\oint_C \mathbf{E}\cdot d\mathbf{l}\right)_i dz = \sum_i \mathcal{E}_i,$$

where η is the longitudinal turn density N/L_b. The index i and its summation account for the several cases of the induced electromotive force that need to be addressed in order to complete the calculation, as shown in (B.1). Because of such partitioning of space with respect to each turn's position, the following cases arise:

1. For $z_m > L_b/2$:
   In this case, the coil is located totally within the lower region of the magnet's magnetic field ($z \leqslant z_m$). Thus $a = -L_b/2$ and $b = L_b/2$ with the integrand belonging to region $z \leqslant z_m$.
2. For $z_m + h_m > L_b/2$ and $-L_b/2 < z_m < L_b/2$:
   In this case, the coil is divided among the lower and middle regions of the magnet's magnetic field. Therefore, it is necessary to compute integrals on those two regions, with integration limits $(a,b) = (-L_b/2, z_m)$ and $(a,b) = (z_m, L_b/2)$ for the integrands belonging to $z \leqslant z_m$ and $z_m \leqslant z \leqslant z_m + h_m$, respectively.
3. For $z_m < -L_b/2$ and $-L_b/2 < z_m + h_m < L_b/2$:
   In this case, the coil is divided among the upper and middle regions of the magnet's magnetic field. Because of this, two integrals must be calculated with integration limits $(a,b) = (-L_b/2, z_m + h_m)$ and $(a,b) = (z_m + h_m, L_b/2)$ for the integrands belonging to $z_m \leqslant z \leqslant z_m + h_m$ and $z > z_m + h_m$, respectively.
4. For $z_m + h_m < -L_b/2$:
   In this case, the coil is located totally within the upper region of the magnet's magnetic field ($z > h_m$). Hence, there is a single integral to be computed with integration limits $a = -L_b/2$ and $b = L_b/2$ for the integrands belonging to $z > z_m + h_m$.

There is an additional case that depends on the relation between L_b and h_m, which is when the magnet is entirely in the domain of the coil. In this case we have the following:

1. If $L_b > h_m$:
   Then $z_m \geqslant -L_b/2$ and $z_m + h_m \leqslant L_b/2$ and the coil is divided among all the regions of the magnet's magnetic field. In consequence, three integrals need to be computed, with integration limits $(a,b) = (-L_b/2, z_m)$, $(a,b) = (z_m, z_m + h_m)$ and $(a,b) = (z_m + h_m, L_b/2)$ for the integrands belonging to $z \leqslant z_m$, $z_m \leqslant z \leqslant z_m + h_m$ and $z > z_m + h_m$, respectively.
2. If $L_b \leqslant h_m$:
   Then $z_m \leqslant -L_b/2$ and $z_m + h_m \geqslant L_b/2$ and the coil is immersed in the middle region of the magnet's magnetic field. The integration limits for the integrand of this region ($z_m \leqslant z \leqslant z_m + h_m$) are $(a,b) = (-L_b/2, L_b/2)$.

We summarize the preceeding reflections in Table B.3. Thereupon we proceed to calculate the resulting expressions. To shorten the calculation, we first integrate with arbirtrary limits a, b the cases of (B.1), and then evaluate the limits presented in Table B.3. The final expression for the induced voltage is given in (3.13).

Table B.3
Integration limits for the calculation of the induction on the coil.

Case	Conditions	Limits (a,b) for region:		
		$z < z_m$	$z_m \leqslant z \leqslant z_m + h_m$	$z > z_m + h_m$
1	$z_m \geqslant \frac{L_b}{2}$	$\left(-\frac{L_b}{2}, \frac{L_b}{2}\right)$	–	–
2	$-\frac{L_b}{2} < z_m < \frac{L_b}{2}$ and $z_m + h_m > \frac{L_b}{2}$	$\left(-\frac{L_b}{2}, z_m\right)$	$(z_m, \frac{L_b}{2})$	–
3	$-\frac{L_b}{2} < z_m + h_m < \frac{L_b}{2}$ and $z_m < -\frac{L_b}{2}$	–	$(-\frac{L_b}{2}, z_m + h_m)$	$(z_m + h_m, \frac{L_b}{2})$
4	$z_m + h_m \leqslant -\frac{L_b}{2}$	–	–	$\left(-\frac{L_b}{2}, \frac{L_b}{2}\right)$
5. Magnet totally within the coil, $L_b > h_m$				
5.1	$z_m + h_m \leqslant \frac{L_b}{2}$ and $z_m \geqslant -\frac{L_b}{2}$	$\left(-\frac{L_b}{2}, z_m\right)$	$(z_m, z_m + h_m)$	$(z_m + h_m, \frac{L_b}{2})$
5. Magnet totally within the coil, $L_b \leqslant h_m$				
5.2	$z_m + h_m \geqslant \frac{L_b}{2}$ and $z_m \leqslant -\frac{L_b}{2}$	-	$\left(-\frac{L_b}{2}, \frac{L_b}{2}\right)$	–

- For $z \geqslant z_m + h_m$:

$$\mathcal{E}_i = \eta \int_a^b \left(\oint_C \mathbf{E}\cdot d\mathbf{l}\right) dz = \eta \int_a^b \left(-\alpha \dot{z}_m \int_0^\infty (e^{h_m k} - 1) e^{k(z_m - z)} J_1(r_m k) J_1(r_b k) dk\right) dz$$
$$= -\alpha\eta\dot{z}_m \int_0^\infty (e^{h_m k} - 1) \frac{e^{k(z_m - a)} - e^{k(z_m - b)}}{k} J_1(r_m k) J_1(r_b k) dk$$

- For $z_m < z < z_m + h_m$:

$$\mathcal{E}_i = \eta \int_a^b \left(\oint_C \mathbf{E}\cdot d\mathbf{l}\right) dz = \eta \int_a^b \left(-\alpha \dot{z}_m \int_0^\infty (e^{k(z - h_m - z_m)} - e^{k(z_m - z)}) J_1(r_m k) J_1(r_b k) dk\right) dz$$
$$= -\alpha\eta\dot{z}_m \int_0^\infty \frac{e^{-k(z_m + h_m)}(e^{bk} - e^{ak}) + e^{k(z_m - b)} - e^{k(z_m - a)}}{k} J_1(r_m k) J_1(r_b k)\ dk.$$

- For $z \leqslant z_m$:

$$\mathcal{E}_i = \eta \int_a^b \left(\oint_C \mathbf{E}\cdot d\mathbf{l}\right) dz = \eta \int_a^b \left(-\alpha \dot{z}_m \int_0^\infty (e^{-h_m k} - 1) e^{k(z - z_m)} J_1(r_m k) J_1(r_b k) dk\right) dz$$
$$= -\alpha\eta\dot{z}_m \int_0^\infty (e^{-h_m k} - 1) \frac{e^{-k z_m}(-e^{ak} + e^{bk})}{k} J_1(r_m k) J_1(r_b k) dk.$$

References

[1] J.A. Paradiso, T. Starner, Energy scavenging for mobile and wireless electronics, Pervasive Comput. IEEE 4 (1) (2005) 18–27, doi:10.1109/MPRV.2005.9. <http://dx.doi.org/10.1109/MPRV.2005.9>.

[2] P.D. Mitcheson, E.M. Yeatman, G.K. Rao, A.S. Holmes, T.C. Green, Energy harvesting from human and machine motion for wireless electronic devices, in: Proceedings of the IEEE 96 (9) (2008) 1457–1486. doi:10.1109/JPROC.2008.927494.

[3] M.S.M. Soliman, E.F. El-Saadany, R.R. Mansour, Electromagnetic mems based micro-power generator, in: Proc. IEEE Int Industrial Electronics Symp, vol. 4, 2006, pp. 2747–2753. doi:10.1109/ISIE.2006.296049.

[4] D. Randjelovic, A. Petropoulos, G. Kaltsas, M. Stojanovic, Z. Lazic, Z. Djuric, M. Matic, Multipurpose mems thermal sensor based on thermopiles, Sensor Actuator A: Phys. 141 (2) (2008) 404–413, doi:10.1016/j.sna.2007.10.043. <http://www.sciencedirect.com/science/article/B6THG-4PYP6YY-7/2/efae3b07b8e560086ab62b80d29bbe13>.

[5] E.M. Yeatman, Applications of mems in power sources and circuits, J. Micromech. Microeng. 17 (7) (2007) S184–S188, doi:10.1088/0960-1317/17/7/S16. <http://dx.doi.org/10.1088/0960-1317/17/7/S16>.

[6] E. Halvorsen, Energy harvesters driven by broadband random vibrations, IEEE/ASME J. Microelectromech. Syst. 17 (5) (2008) 1061–1071, doi:10.1109/JMEMS.2008.928709.

[7] P.D. Mitcheson, T.C. Green, E.M. Yeatman, A.S. Holmes, Architectures for vibration-driven micropower generators, J. Microelectromech. Syst. IEEE 13 (3) (2004) 429–440, doi:10.1109/JMEMS.2004.830151.

[8] J.D. Jackson, Classical Electrodynamics, 3rd ed., Wiley, 1999.

[9] W.H., S. A. Teukolsky, W. T. Vetterling, B. P. Flannery, Numerical Recipes 3rd Edition: The Art of Scientific Computing, 3rd Edition, Cambridge University Press, 2007. URL <http://www.amazon.com/exec/obidos/redirect?tag=citeulike07-20&path=ASIN/0521880688>.

[10] G.N. Watson, A Treatise on the Theory of Bessel Functions, Cambridge University Press, 1944.

[11] J. ao Pedro, N. Sadowski, Electromagnetic Modeling by Finite Element Methods, 1st ed., CRC Press, 2003. <http://www.amazon.com/exec/obidos/redirect?tag=citeulike07-20&path=ASIN/0824742699>.

[12] T.-S. Tran, G. Meunier, P. Labie, J. Aime, Comparison of FEM-PEEC coupled method and finite-element method, IEEE Trans. Magnetics 46 (4) (2010) 996–999, doi:10.1109/TMAG.2009.2037953. <http://dx.doi.org/10.1109/TMAG.2009.2037953>.